

Evidence of Lattice Strain as a Precursor to Superconductivity in $\text{BaPb}_{0.75}\text{Bi}_{0.25}\text{O}_3$

M Bharath,¹ Jaskirat Brar,¹ Himanshu Pant,¹ Asif Ali,² Sakshi Bansal,² Ravi Shankar Singh,² and R Bindu¹

¹*School of Physical Sciences, Indian Institute of Technology Mandi, Kamand, Himachal Pradesh-175005, India*

²*Department of Physics, Indian Institute of Science Education and Research, Bhopal, Madhya Pradesh-462066, India*

In this work, we have investigated the precursor effects to superconductivity in $\text{BaPb}_{0.75}\text{Bi}_{0.25}\text{O}_3$ using temperature dependent resistivity, x-ray diffraction technique and photoemission spectroscopy. The present compound exhibits superconductivity around 11 K (T_C). The synthesis procedure adopted is much simpler as compared to the procedure available in the literature. In the temperature range (10 K–25 K) i.e. above T_C , our results show an increase in both the orthorhombic and tetragonal strain. The well screened features observed in Bi and Pb $4f_{7/2}$ core levels are indicative of the metallic nature of the sample. The compound exhibits finite intensity at the Fermi level at 300 K and this intensity decreases with decrease in temperature and develops into a pseudogap; the energy dependence of the spectral density of states suggests disordered metallic state. Furthermore, our band structure calculations reveal that the structural transition upon Pb doping results in the closing of the band gap at the Fermi level.

PACS numbers: 61.05.C-, 74.25.Jb

I. INTRODUCTION

The lead doped BaBiO_3 , $\text{BaPb}_{1-x}\text{Bi}_x\text{O}_3$ (BPBO), is a well-known 3-dimensional perovskite, which exhibits superconductivity for bismuth compositions in the range $0.15 \leq x \leq 0.35$ ¹. This family of compounds has attracted much attention because of its relatively high transition temperature ($T_C \sim 13$ K, at $x = 0.25$ ²), despite the low carrier concentration³. Unlike the cuprates or lanthanides, BPBO family of superconductors are (i) three-dimensional, (ii) without transition metal ions like Cu, La, etc, and (iii) non-magnetic. In the superconducting compositions, the compound is diphasic, with the co-existence of the tetragonal and orthorhombic phases^{1,4}; the volume fraction of tetragonal phase dictates the T_C , thus being the superconducting phase. Recently, Nicoletti et al.⁵ have shown that a short range CDW order exists adjacent to the superconducting phase (i.e., above ~ 7 K) in superconducting $\text{BaPb}_{0.78}\text{Bi}_{0.22}\text{O}_3$. Further, recent study by Parra et al.⁶, shows that an electronic reorganization into a 2D granular superconductor takes place when BPBO approaches the superconductor-insulator transition before ultimately transforming to an insulator. Superconductivity is generally seen adjacent to exotic symmetry-breaking ground states, like AFM and CDW orders⁵. Usually, a complex but subtle interplay between spin, charge, crystal and electronic structures shape the resulting electronic properties. BPBO, which manifests such emergent electronic properties, is an ideal candidate to engineer novel superconducting devices such as quantum computing circuits⁷.

The crystal structure of superconducting compositions have been a major point of confusion – Cox and Sleight⁸ have reported that the compound is tetragonal in the range $0.05 < x < 0.35$; Khan et al.⁹ observe that the compound has a distorted orthorhombic crystal structure belonging to the $Cmm2$ phase for all compositions, whereas, Oda et al.¹⁰ concluded that the compound is orthorhombic for all compositions with $x < 0.9$ along with

a structural transition from an orthorhombic to a monoclinic phase at about 160 K in case of $\text{BaPb}_{0.75}\text{Bi}_{0.25}\text{O}_3$; in a later study, Asano et al.¹¹ and Oda et al.¹² proposed that the differences in the sample preparation techniques could result in the compounds stabilising in either orthorhombic or tetragonal phase, each having a distinct T_C .

Investigations of the phase separation of $\text{BaPb}_{1-x}\text{Bi}_x\text{O}_3$ by Giraldo-Gallo et al. using high quality single crystals¹³ have lead to the observation that the structural dimorphism takes the form of partially disordered nanoscale stripes for optimal composition of $x \approx 0.24$. As the bismuth composition deviates from its optimal value, the volume of tetragonal phase reduces and the tetragonal stripes reduce to islands embedded in a matrix of orthorhombic $\text{BaPb}_{1-x}\text{Bi}_x\text{O}_3$. Point-contact spectroscopic measurements performed on $\text{BaPb}_{1-x}\text{Bi}_x\text{O}_3$ ($0 \leq x \leq 0.28$) indicate that the metal-insulator transition (MIT) is driven by disorder¹⁴. Magnetoresistance studies performed on $\text{BaPb}_{0.75}\text{Bi}_{0.25}\text{O}_3$ epitaxial thin films grown on LaLuO_3 by Harris et al.¹⁵, show superconducting fluctuations in epitaxial thin films well above T_C ; and in case of the thickest films with thickness above 100 nm these fluctuations were observed till 27 K.

Several photoemission spectroscopy measurement studies on $\text{BaPb}_{1-x}\text{Bi}_x\text{O}_3$ have been reported, some performed on single crystals^{16–19}, and few more of polycrystalline samples^{20–22}. Most studies do not reveal any charge disproportionation in the compound^{16–20}, notable exception being Kostikova et al.²¹. and Korolkov et al.²², who noticed the presence of both Pb^{II} and Pb^{IV} , along with Bi^{III} and Bi^{V} in their compound under study – $\text{BaPb}_{0.8}\text{Bi}_{0.2}\text{O}_3$. Room temperature (RT) x-ray photoelectron spectroscopic (XPS) studies by Wertheim et al.¹⁶ and Sakamoto et al.²⁰ show no indication of any density of states (DOS) at Fermi level (E_F). However, later ultraviolet photoemission studies (UPS) by Matsuyama et al.¹⁷ (at RT and 180 K), and Namatame et

al.¹⁹ (at liquid-nitrogen temperature (LNT)) indicate a finite DOS at E_F . The UPS studies by Matsuyama et al.¹⁷ show that $\text{BaPb}_{0.85}\text{Bi}_{0.15}\text{O}_3$ has a clear Fermi-edge structure characteristic of normal metal; suggesting that the superconductivity would be driven by Cooper pairing of electrons in the Fermi-liquid states. According to the BCS theory, good metals do not become superconductors because of weak-electron phonon coupling, which makes their claim a very interesting one. It is also important to note that their measurements were done at 180 K, a temperature significantly higher than the T_C of the compound. The electronic structure studies by Namatame et al.¹⁹ was performed at LNT in an attempt to obtain a picture of the electronic structure of $\text{BaPb}_{1-x}\text{Bi}_x\text{O}_3$ for a wide range of compositions. Further, studies exploring effects such as superconducting fluctuations discovered by Harris et al.¹⁵ indicate a presence of precursor effects before the onset of bulk superconductivity. To understand the manifestation of co-existence of two structural phases in the electronic structure or precursor effects to superconductivity in $\text{BaPb}_{0.75}\text{Bi}_{0.25}\text{O}_3$ we have carried out temperature dependent crystal structure and electronic structure studies on the compounds above T_C .

Another interesting aspect of the $\text{BaPb}_{1-x}\text{Bi}_x\text{O}_{3-\delta}$ series is the strong dependence of the superconductivity on the oxygen content in the sample²³. The authors found that an oxygen deficiency of greater than $\delta = 0.11$ destroyed the superconductivity. Hence, an elaborate preparation procedure is generally used to ensure that sample is well-oxygenated. The typical preparation route is via solid state reactions of powdered raw materials – BaCO_3 , Pb_3O_4 and Bi_2O_3 – taken in stoichiometric proportions. These raw materials are mixed in ethanol and ground well using a ball-milling machine. The mixture is then heated at 720 °C for 12 h under flowing oxygen. Further, the calcined sample is ground again, pressed into a pellet and then sintered at 800 °C for 12 h, in oxygen atmosphere.

In this paper, we investigate the possible precursor effects leading to the superconductivity. We present a detailed investigation of temperature dependent resistivity, crystal structure and electronic structure studies on the compound under study. The electrical transport and magnetic susceptibility measurements indicate a superconducting transition around 11 K. Further, these studies reveal that the disorder plays a very important role in the electrical resistivity and the electronic structure of the compound. The spectral DOS near the Fermi level displays a square-root of energy dependence indicating the compound to be a disordered metal above T_C . The temperature evolution of the symmetrised spectral density of states indicates the development of a disorder-induced pseudogap at the Fermi level. Band structure calculations performed using the TB-mBJ correlation functional indicates that the monoclinic $I2/m$ to tetragonal $I4/mcm$ structural phase transition upon Pb doping of the parent compound plays a major role in the closing of the band gap observed in the compound under study.

Additionally, we have adopted a much simpler synthesis procedure as compared to the ones available in the literature.

II. EXPERIMENTAL

The polycrystalline samples of $\text{BaPb}_{0.75}\text{Bi}_{0.25}\text{O}_3$ were prepared via solid state route from BaCO_3 , Bi_2O_3 and Pb_3O_4 . The raw materials were first preheated at 450 °C for 2 hours to remove any traces of moisture absorbed by them. The proper stoichiometric ratios of the raw materials were then ground thoroughly in a agate mortar for 24-48 hours. This finely ground powder was then calcined in a box furnace at 900 °C for 48 hours. The heating rate was maintained at 5 °C/min and the samples were allowed to cool down to room temperature naturally inside the box furnace. The calcined powders were then sintered in the box furnace at 900 °C for around 150 hours, with intermediate grindings every 24 hours. The final sintering was performed at 950 °C. After each grinding, the powders were then pressed into pellets of 10 mm diameter under a hydrostatic pressure of 5 tons. It was found that covering the pellets with a thin layer of powder of the sample ensured a good stoichiometric compound, and prevented the escape of Bi or Pb from the surface of the pellet. It is to be noted that despite not sintering the sample in oxygen atmosphere, we were able to obtain a superconducting transition.

The temperature dependent *xrd* (T-XRD) measurements were performed using Rigaku's Smart Lab x-ray diffractometer powered by a 9kW rotating anode x-ray generator. The T-XRD patterns were collected using Cu K_α radiations and were collected in the 2θ range of 19° to 87° at a scanning speed of 1° per minute with a step size of 0.02°. The Magnetic Properties Measurement System (MPMS) from Quantum Design, Inc. was used in the measurement of temperature dependent dc magnetization measurements. The measurement was performed at an applied magnetic field of 0.5 T, in the temperature range of 300K to 2K. Electrical resistivity measurements were performed on the sample using Physical Properties Measurement System (PPMS) setup from Quantum Design, Inc, in the same temperature range, using a standard 4-probe DC resistivity method. The probes were attached to the sample using high quality silver paste, and the data collection was done during the cooling cycle. The field emission scanning electron microscopy (FE-SEM) micrographs were procured using Nova Nano SEM-450 at room temperature at a chamber pressure of 10^{-5} mbar, with a scanning voltage of 10 kV.

The temperature dependent photoemission spectra were collected on Scienta R4000 hemispherical analyser using a monochromatic Al K_α (1486.6 eV) x-ray source, He I (21.2 eV), and He II (40.8 eV) ultraviolet radiations at various temperatures between 300 K to 30 K. The binding energy scale was calibrated by measuring the Fermi level of Ag pellet, cleaned in situ by argon

ion sputtering, using monochromatic Al K_α and HeI. A clean sample surface was obtained by fracturing the mounted samples in a chamber having vacuum better than 7×10^{-11} mbar. The base pressure during the measurement was 5×10^{-11} mbar.

III. COMPUTATIONAL

Band structure calculation using self-consistent full potential linear augmented-plane-wave (LAPW) were performed for $\text{BaPb}_{0.75}\text{Bi}_{0.25}\text{O}_3$ using the code implemented in Elk²⁴. We have used local density approximation (LDA)²⁵ for the exchange potential and Tran-Blaha modified Becke-Johnson (TB-mBJ) potential²⁶ for the correlation part. The calculations were performed using the structural parameters obtained from the refinement of the *xrd* patterns of *I4/mcm* phase of $\text{BaPb}_{0.75}\text{Bi}_{0.25}\text{O}_3$ taken at room temperature. A $1 \times 1 \times 1$ supercell was constructed and one atom of Pb was replaced by Bi, to account for the 75% doping of Pb at the Bi-site. The muffin-tin shape approximation for the potential well in the crystal lattice employed in the calculations used radii of 2.8, 2.56, 2.43 and 1.43 bohr for Ba, Bi, Pb and O, respectively. The difference in total energy required for the termination of self-consistent cycles was set to be less than 10^{-4} Hartree/cell. In order to understand the evolution of the states at E_F , we have also performed TB-mBJ calculations on BaBiO_3 using the structural parameters of $\text{BaPb}_{0.75}\text{Bi}_{0.25}\text{O}_3$, using a muffin-tin radii of 2.8, 2.29 and 1.72 bohr for Ba, Bi and O, respectively.

IV. RESULTS AND DISCUSSIONS

A. General Characterization

Figure 1(a) shows the crystal structure of the compound under study; also shown are the Bi(Pb)-O-Bi(Pb) angles of the apical and basal planes of the two phases. Panels (b) and (c) for the same figure (1) show FE-SEM micrographs of the $\text{BaPb}_{0.75}\text{Bi}_{0.25}\text{O}_3$ pellet. The average grain size was estimated to be $\sim 8 \mu\text{m}$.

In figure 2, we show the typical Rietveld fitting of the *xrd* patterns of $\text{BaPb}_{0.75}\text{Bi}_{0.25}\text{O}_3$ collected at 10 K and 300 K. A two-phase Rietveld refinement, consisting of tetragonal *I4/mcm* phase and orthorhombic *Ibmm* phase, has been performed to fit the experimental data; the crystal structure and the room temperature lattice parameters are in line with the earlier works^{1,4,5,13}. The absence of unindexed peaks points to the purity of the sample. The lattice parameters and atomic positions obtained from the refinement of the patterns collected at 300 K and 10 K are shown in Table I.

The quality of fit, when modelled using a single phase – either tetragonal *I4/mcm* or orthorhombic *Ibmm* – is significantly lower as compared to the two-phase fit. The inset (b1) of figure 2(b) shows the fit of the peaks in

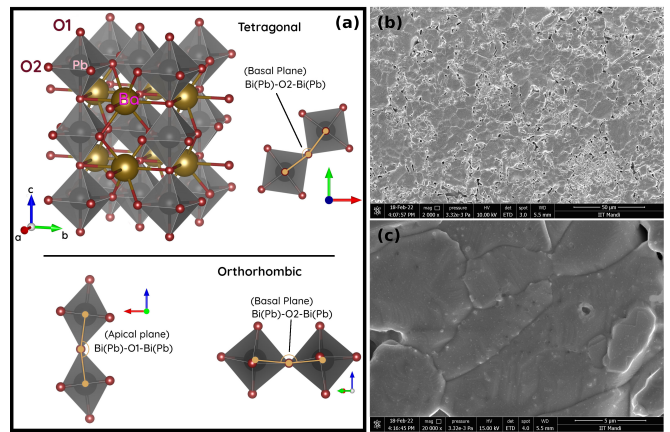


FIG. 1: (Color online) (a) Crystal structure of $\text{BaPb}_{0.75}\text{Bi}_{0.25}\text{O}_3$ – upper panel shows the structure of the tetragonal phase along with the $\text{Bi(Pb)}-\text{O}_2-\text{Bi(Pb)}$ angle between the two $\text{Bi(Pb)}-\text{O}_6$ octahedra in the basal plane. The lower panel shows the $\text{Bi(Pb)}-\text{O}_1-\text{Bi(Pb)}$ angle along the apical plane and $\text{Bi(Pb)}-\text{O}_2-\text{Bi(Pb)}$ angle along the basal plane in case of orthorhombic phase. (b), (c) show the FE-SEM micrographs of $\text{BaPb}_{0.75}\text{Bi}_{0.25}\text{O}_3$ sintered pellets taken at 2000x and 20000x magnifications, respectively.

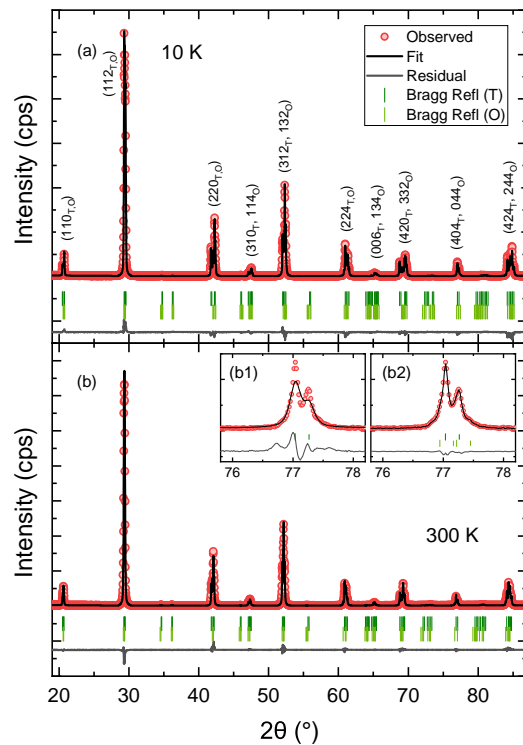


FIG. 2: (Color online) Rietveld refinement of *xrd* patterns collected at (a) 10 K and (b) 300 K. The fitting is performed using two phases – *I4/mcm* and *Ibmm* – at both temperatures. The dark green ticks indicate the Bragg reflections arising from the tetragonal *I4/mcm* phase, and the light green ticks from the orthorhombic *Ibmm* phase. Inset (b1) and (b2) show the fit of the peaks in the range $76^\circ \leq 2\theta \leq 78^\circ$ when modelled using a single *I4/mcm* phase, and two phases (*I4/mcm* and *Ibmm*) respectively.

TABLE I: The lattice parameters, and atomic positions of I4/mcm and Ibmm phases obtained from the two-phase refinement of the spectra collected at 300 K and 10 K. The Wyckoff positions of Ba is 4b, Bi/Pb is 4c, O1 is 4a and O2 is 8h in tetragonal phase. In case of the orthorhombic phase these atoms occupy 4e, 4a, 4e, and 8g positions, respectively.

	Tetragonal Phase		Orthorhombic phase	
	10 K	300 K	10 K	300 K
Lattice parameters				
a (Å)	6.02815	6.05055	6.07851	6.08959
b (Å)	-	-	6.04651	6.06051
c (Å)	8.62396	8.60776	8.51402	8.55560
Atomic Positions				
Ba	x		0.48983	0.50653
O1	x		0.0034	0.0472
O2	x	0.26216 0.22212		
	y	0.76216 0.72212		
	z	0 0	0.9892	0.6102

the range $76^\circ \leq 2\theta \leq 78^\circ$ when modelled using a single tetragonal phase. A similar fit is observed when the *xrd* patterns are refined using a single orthorhombic phase (not shown). Inset (b2) of figure 2(b) shows the peaks in the range when fit using a diphasic model. A sample with tetragonal symmetry shows a single pair of (404) peak (corresponding to Cu $K_{\alpha 1}$ and Cu $K_{\alpha 2}$)²³. On the other hand, in case of orthorhombic symmetry, this peak splits into (404) and (044). To ensure a proper fit, it is necessary to model data using two phases, which result in the decomposition of twin peaks into its 6 constituent peaks – one pair corresponding to (404) reflection from tetragonal phase, one pair each corresponding to (404) and (044) reflections from the orthorhombic phase – thus indicating the coexistence of I4/mcm and Ibmm phases.

In figure 3(a), we show the resistivity versus temperature data for the compound under study. As the temperature drops, the resistivity gradually increases till ~ 250 K, below which a change of slope is observed. The resistivity increases rapidly until ~ 10.5 K (T_C), below which it drops sharply indicating the onset of superconductivity, as seen in the inset of figure 3(a). The figure 3(b) shows the field-cooled (FC) magnetic moment of the sample as function of temperature. As reported in the literature^{27,28}, the sample is diamagnetic in the entire temperature range. The magnetic moment shows sharp drop at around ~ 11 K indicating the onset of the superconducting transition. The combined resistivity and dc magnetic moment measurements suggest the onset of superconductivity at $T_C \approx 11$ K.

Figures 4(a)-(b) illustrate the fit of the resistivity data in two temperature ranges, using different models. The resistivity data in figure 3(a) is roughly divided into 3 regions based on this. In region 1, (~ 250 K - 300 K), the electrical transport is dominated by activated behaviour, which is appreciable when sufficient thermal energy is

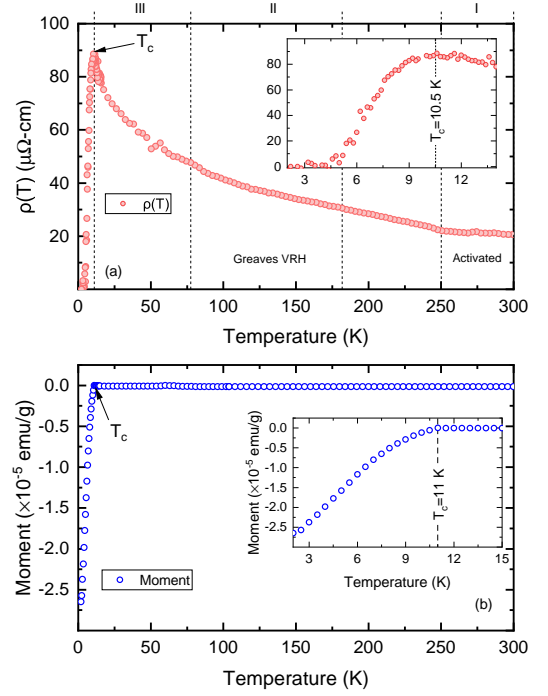


FIG. 3: (Color online) (a): Variation of resistivity with temperature of BaPb_{0.75}Bi_{0.25}O₃. The inset shows the closer view of $\rho(T)$ and ρ_{300} temperature range 2 K to 15 K. In both graphs, the open circles represent the experimentally observed data, and (b) Variation of magnetic moment with temperature of BaPb_{0.75}Bi_{0.25}O₃. The inset shows the closer view of magnetic moment in the temperature range 2 K to 15 K.

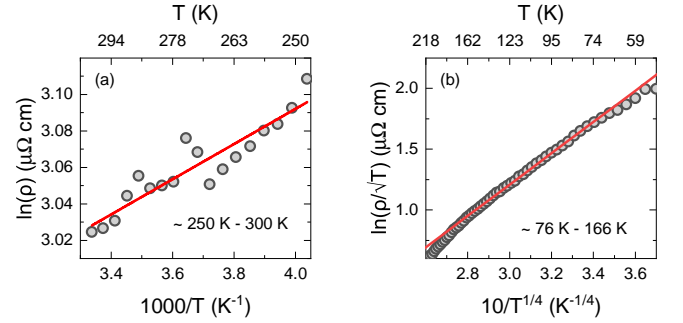


FIG. 4: (Color online) Variation of resistivity demonstrating (a) Arrhenius behaviour in the temperature range 300 K to 250 K; (b) Greaves' variable-range hopping conduction behaviour in the temperature range below 170 K to 66 K.

available for the electron to be excited across the band gap^{29–31}. It is important to note that the studies by Uchida et al.³², indicate that temperature dependence of normal-state resistivity of BaPb_{1-x}Bi_xO₃ is like that of semiconductors for $x > 0.20$. Figure 4(a) shows the variation of $\log \rho$ as a function of $1/T$, modelled by equation 1.

$$\rho(T) = \rho_0 e^{E_G/k_B T} \quad (1)$$

where, ρ_0 is a pre-exponential factor, E_G is the activation

energy, and $k_B = 1.38 \times 10^{-23} \text{ JK}^{-1}$ is the Boltzmann's constant. From the straight line fit of the data, we obtain an activation energy of $E_g = 7.6 \text{ meV}$.

As the temperature drops below 250 K, it's not possible to model the data using Arrhenius-type behaviour. We observe a transition of the resistivity behaviour from Arrhenius to variable range hopping (VRH). Mott variable-range hopping model has a characteristic temperature dependence of resistivity^{33,34} given by

$$\rho(T) = \rho_0 e^{(T_M/T)^{1/(p+1)}} \quad (2)$$

where p is a parameter that describes the dimensionality of the conduction in the system, and ρ_0 is a pre-exponential constant. T_M is the characteristic Mott temperature, which describes the energy barrier of an electron hopping from one localized state to another, given by the equation 3.

$$T_M = \frac{18.1}{k_B \xi^3 N(E_F)} \quad (3)$$

Here, it is important to note that it was not possible to fit the entire temperature range below 250 K, till the T_C , with a single curve. It was necessary to split them into separate regions with distinct characteristic temperatures and localization lengths. However, while we were able to fit the data using equation 2 mathematically, we found that the ratio of mean hopping distance to electron localization length, given by equation 4, is much less than 1, which is an indication that equation 2 is not applicable in our case³⁵.

$$R_M/\xi = \frac{3}{8} \left(\frac{T_M}{T} \right)^{1/4} \quad (4)$$

In the intermediate temperature range, the resistivity data can be fit using Greaves VRH³⁰. The acoustic phonon contribution to the resistivity^{29,30}, takes the form as given in equation 5,

$$\rho(T) = AT^{1/2} e^{(T_G/T)^{1/4}} \quad (5)$$

where, A is the pre-exponential constant and T_G is the characteristic temperature of Greaves VRH.

For Greaves VRH to be valid, the plot of $\ln(\rho/\sqrt{T})$ versus $T^{-1/4}$ should be linear. In this intermediate temperature range ($\Theta_D/4 < T < \Theta_D/2$) where the deviation from the fit is observed has been taken to be $\Theta_D/2$ in the higher temperature limit, and $\Theta_D/4$ in the lower temperature limit^{31,36}. Below this temperature, we have been unable to model the resistivity using this equation. Thus, the best fit was observed in the temperature range $\sim 76 \text{ K}$ to 166 K , and we obtained the characteristic temperature of $T_G = 27563 \text{ K}$. Using the value of $N(E_F) = 2.2 \times 10^{21} \text{ states/cm}^3$, as reported by Kitazawa, et al.³⁷, we obtain the electron localization length of $\xi = 15.49 \text{ \AA}$. The deviation of the resistivity from the fit begins at $\sim 76 \text{ K}$ at the lower end, and $\sim 166 \text{ K}$ at the higher end. Thus, we may estimate that the Debye temperature of the compound lies between $\sim 304 \text{ K}$ to 332 K .

B. Temperature dependent *xrd* studies

To understand the structural link with the transport properties and understand the behaviour of phase separation, we have carried out temperature dependent *xrd* on the compound. Figures 5-7 show the variation of the lattice parameters, bond lengths, bond angles, lattice strain, and unit cell volume with temperature. The *xrd* patterns were analysed using Rietveld profile refinement and the structural parameters were obtained as a function of temperature. The goodness of fit obtained is in the range $1.45 - 1.63$ for all temperatures. As the temperature drops from 300 K to 10 K , we observe that the number of peaks remain the same. This suggests the absence of any structural transitions at lower temperatures, in contrast to some of the earlier studies^{10,11}. Moreover, we observe that the fraction of the tetragonal phase is $\sim 70\%$, and is largely temperature independent (see figure 7(a)).

Keeping these results in mind, revisiting the resistivity studies of the previous section gives an opportunity to understand the high transition temperature of VRH from Arrhenius type behaviour. Firstly, at low temperature, the thermal energy available for excitation of electron is insufficient, thus leading the electrical transport behaviour away from activated behaviour. In such a scenario, it is favorable for the electron to hop to a site farther than the nearest neighbour with a lower potential, giving rise to observed VRH behaviour³¹. Furthermore, we hypothesize that this high transition temperature is due to the role of disorder in the system. Two leading contributions to disorder are (a) the structural phase coexistence of orthorhombic and tetragonal phases at all temperatures, with fraction of the tetragonal phase constant at $\sim 70\%$, and largely temperature independent, and (b) the composition lying within the transition region between metal and semiconducting regions. The work on $\text{BaPb}_{1-x}\text{Bi}_x\text{O}_3$ by Uchida et al.³² suggests that the compound under study lies in the region where both metal and semiconducting regions co-exist.

Figures 5(a) and 5(b) illustrate the variation of the lattice parameters of $I4/mcm$ and $Ibmm$ phases with temperature. In order to facilitate the comparison of the structural data with resistivity measurements, the entire temperature range have been divided into three regions, identical to that in figure 3(a). In the activated region, the a parameter of the tetragonal phase, decreases by 0.0014% , whereas c increases by 0.001% . As the temperature drops to region II, the decrement in a is 0.0022% , and the increment in c is 0.001% . In region III, the lattice parameters are nearly constant within the range of experimental error.

The antiphase $\text{Bi(Pb)}\text{-O}_6$ octahedral rotations about the c -axis increase with decreasing temperature. The decreasing $\text{Bi(Pb)}\text{-O}_2\text{-Bi(Pb)}$ bond angle results in the contraction of the a parameter. This reduction in the bond angle effectively contracts the interstitial volume around the Barium atom, thus increasing the $\text{O}_1\text{-Ba-O}_2$ angle, which drives the increase in the c parameter with

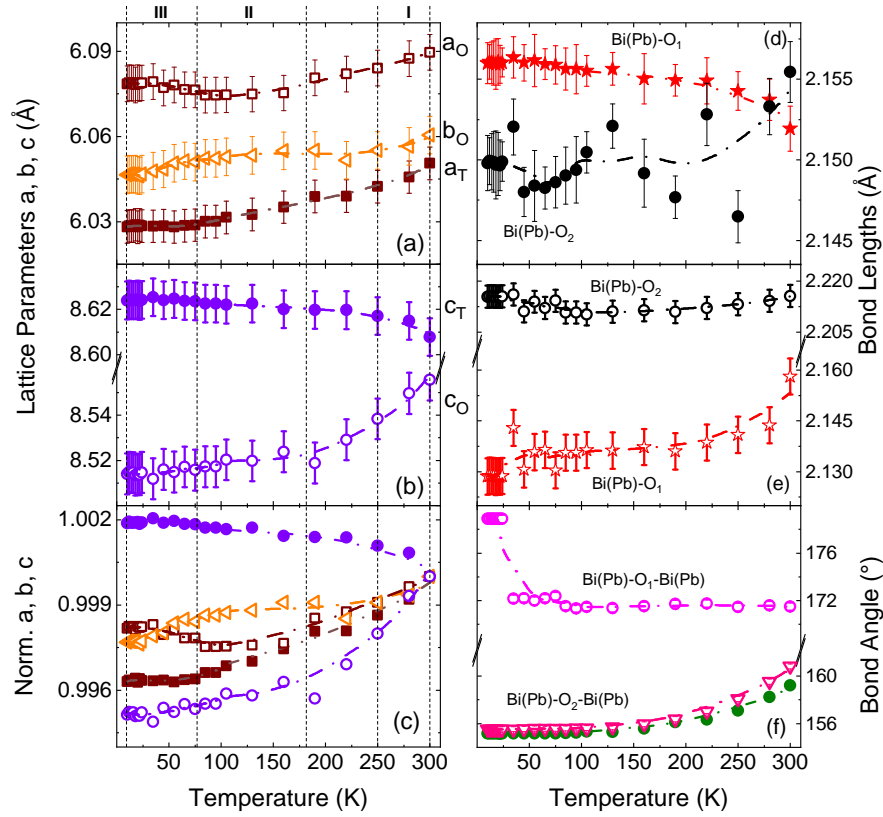


FIG. 5: (Color online) Variation of lattice parameters with temperature for tetragonal phase (closed symbols) and orthorhombic phase (open symbols) of $\text{BaPb}_{0.75}\text{Bi}_{0.25}\text{O}_3$. (a) and (b) show the evolution of a (square), b (triangle) and c (circle) lattice parameters, respectively. (c) shows the temperature variation of the lattice parameters normalized with respect to their respective values at RT. (d) shows the variation in bond lengths of Bi/Pb and the apical (star) and basal (circle) oxygens in the I4/mcm phase. (e) shows the variation in bond lengths of Bi/Pb and the apical (star) and basal (circle) oxygens in the Ibmm phase. (f) shows the variation of the angle between two Bi(Pb) and apical and basal oxygens. Dashed lines are a visual guide indicating the overall behaviour of the various parameters.

decreasing temperature.

The lattice parameters of the Ibmm phase, however, paint a more complex picture. The figure 5(a) and (b) respectively show the variation of a , b , and c parameters of the Ibmm phase. The lattice parameters a and c reduce monotonically until ~ 75 K, dictated by the reducing bond lengths and bond angles; further, b decreases monotonically until the beginning of region II, and remains constant in region II. Below ~ 75 K, a increases, while b decreases; c remains nearly constant. The interplay between the bond lengths and bond angles leading to the observed behaviour of the lattice parameters are easily understood from graphs in panels (e) and (f) of figure 5.

From figures 6(a) and (b), we clearly observe that the nature of $\text{Bi(Pb)}\text{-O}_6$ octahedra is different in the two phases. In the case of tetragonal phase, there are two long apical Bi-O bonds and four short basal Bi-O bonds, while in the case of orthorhombic phase, the trend is reversed. It is interesting to note that, Gallo et al.¹³, have observed that the phase separation takes the form of partially disordered nanoscale stripes. It is possible that the

difference in the nature of distortion could be one of the reasons for such stripes. These experiments were carried out by the authors on single crystalline $\text{BaPb}_{0.75}\text{Bi}_{0.25}\text{O}_3$ and have observed nanoscale structural phase separation.

To understand the nature of phase separation in the present work, one can propose two scenarios^{38,39} (a) two phases coexisting in the same grain; (b) two phases lying in two different grains. In the first scenario, it is expected that one phase grows at the cost of the other while in the second case the phase fraction remains the same. Towards this, we have calculated the average size of the structural phases as a function of temperature using Scherrer formula⁴⁰ (equation 6).

$$B = \frac{K\lambda}{\beta \cos \theta} \quad (6)$$

where, $K = 0.9$ is a constant, $\lambda = 1.5405 \text{ \AA}$ is the x-ray wavelength, β is the FWHM of the peak at angle 2θ . Our results show that the size of the structural phases remains the same through temperature range of study. This behaviour suggests the second scenario proposed above. However, temperature dependent transmission electron

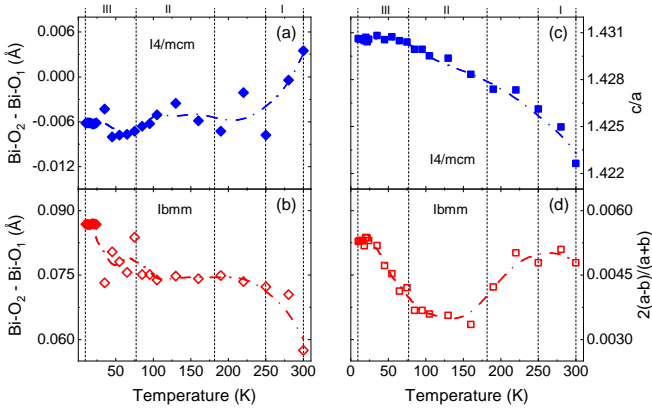


FIG. 6: (Color online) Temperature variation of (a) basal and apical bond length difference in tetragonal phase, (b) basal and apical bond length difference in orthorhombic phase, (c) tetragonal strain, c/a and (d) orthorhombic strain, $2(a-b)/(a+b)$. Dashed lines are a visual guide indicating the overall behaviour of the various parameters.

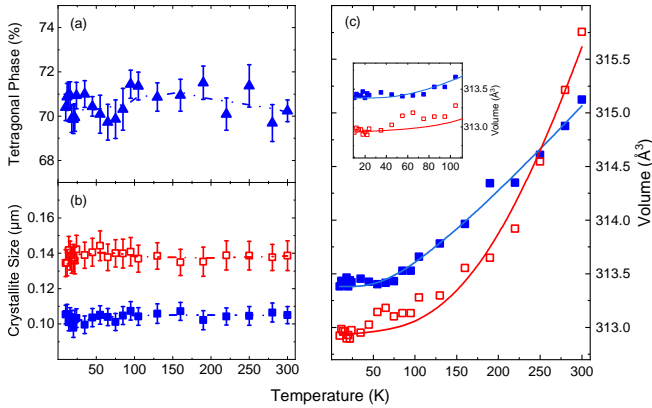


FIG. 7: (Color online) The temperature variation of (a) tetragonal phase fraction (b) crystallite size of tetragonal (closed squares) and orthorhombic (open squares) phases calculated from the Scherrer equation. (c) volumes of tetragonal and orthorhombic phases (closed and open square, respectively), and the Debye fit to the anharmonic part of the lattice contribution to the unit cell volumes (solid lines). The inset shows the close-up of the volumes in the temperature range 10 K to 110 K.

microscopy (TEM) studies will be helpful to unravel the nature of phase separation in this polycrystalline compound.

Graphs in figure 6(c) and (d) show the temperature variation of tetragonal and orthorhombic strain. In the forth coming section, we will be using the term lattice strain synonymous to tetragonal/orthorhombic strain. In the tetragonal phase (figure 6(c)), we observe the lattice strain increases with decrease in temperature and in the orthorhombic phase (figure 6(d)), the lattice strain decreases until around 125 K and below this temperature it is found to increase. It is interesting to note that in the temperature range close to T_C , the lattice strain is

TABLE II: Parameters of Debye fit obtained from fitting of tetragonal and orthorhombic phase volumes.

Phase	V_0	$(9\gamma Nk_B)/B$	Θ_D
Tetragonal	313.38	0.026	330.4
Orthorhombic	312.92	0.098	916.8

maximum possibly playing a role as precursor for superconductivity. Such behaviour has been observed in the case of $\text{YBa}_2\text{Cu}_3\text{O}_7$ compound⁴¹, where the orthorhombic strain is found to be maximum around T_C with little to no anomaly in the unit cell volume. However, in the present study we observe an anomaly in the unit cell volume around 35 K and 65 K, in the tetragonal and orthorhombic phases, respectively, (see figure 7(c)). In this figure, the anharmonic part of the lattice contribution to the unit cell volumes was obtained by fitting with Debye model, as given by equation 7.

$$V \approx V_0 + \frac{9\gamma Nk_B}{B} T \left(\frac{T}{\Theta_D} \right)^3 \int_0^{\Theta_D/T} \frac{x^3}{e^x - 1} dx \quad (7)$$

where, V_0 is the volume at absolute zero, N is the number of atoms per unit cell, γ is the Grünesian parameter and Θ_D is the Debye temperature. The three fitting parameters – V_0 , $(9\gamma Nk_B)/B$ and Θ_D – were determined using the least square fitting, are shown in table II. We readily see that the $\Theta_D^{\text{tetra}} = 330.4$ K, the Debye temperature of the majority phase fraction of the compound, obtained from the fit matches well with the estimate obtained from the resistivity data, as previously discussed.

V. ELECTRONIC STRUCTURE STUDIES

The results discussed thus far indicate that the disorder plays a very important role in the sample, especially in the region just above T_C . Signature of disorder is visible not only in transport measurements, but also is expected to manifest in electronic structure. According to BCS theory, good conductors do not show superconductivity because of weak electron phonon coupling. In the present compound, the observed resistivity values lie in the range of metals. It will be interesting to study the temperature dependent behaviour of the electronic states close to the Fermi level and also behaviour of core levels prior to T_C . To visualize and understand the electronic structure of $\text{BaPb}_{1-x}\text{Bi}_x\text{O}_3$, we have performed photoemission spectroscopy measurements on our sample at various temperatures between 300 K and 30 K, using Al K_α x-ray radiation, He I and He II ultraviolet radiations. Figure 8 shows the core levels of the compound collected at RT and 30 K.

A. Core level studies

Panels (a)–(e) of figure 8 show the core level spectra of Ba $3d_{5/2}$, Ba $4d_{5/2}$, O $1s$, Bi $4f_{7/2}$, and Pb $4f_{7/2}$,

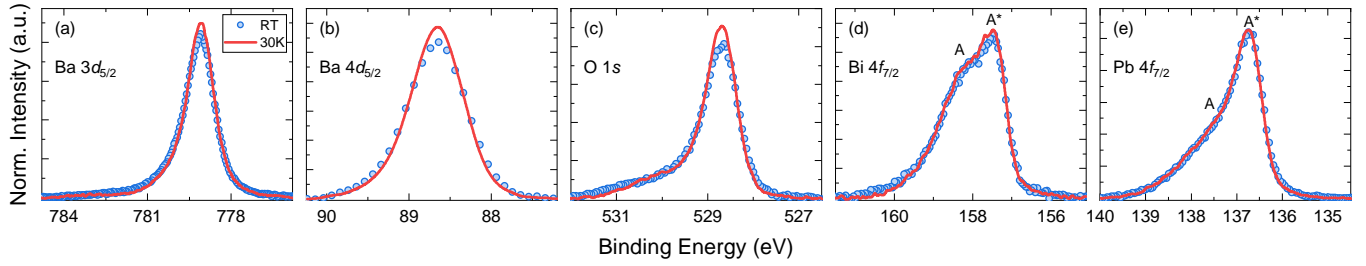


FIG. 8: Core level spectra of $\text{BaPb}_{0.75}\text{Bi}_{0.25}\text{O}_3$ at 300 K (open circles) and 30 K (solid lines). (a) Ba $3d_{5/2}$ (b) Ba $4d_{5/2}$ (c) O $1s$ (d) Bi $4f_{7/2}$ and (e) Pb $4f_{7/2}$. The labels A and A* in panels (d) and (e) indicate the positions of poorly-screened and well-screened peaks, respectively.

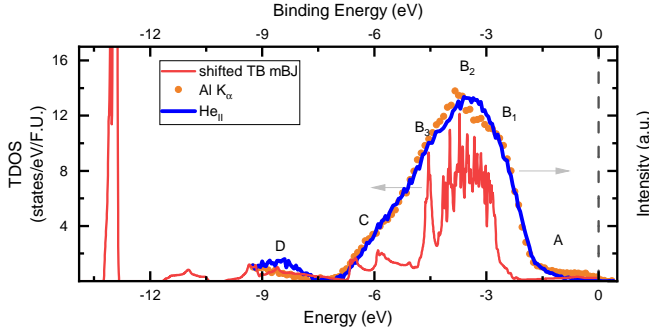


FIG. 9: (Color online) A comparison of Al K_{α} spectrum (closed circles, orange), HeII spectrum (solid line, blue) and the total DOS (solid line, red) obtained from the TB-mBJ calculations performed on tetragonal phase of $\text{BaPb}_{0.75}\text{Bi}_{0.25}\text{O}_3$. The total DOS is shifted by -0.8 eV to match the experimental Al K_{α} spectrum. The inset shows the finite DOS at Fermi level using Al K_{α} radiation.

respectively, at 300 K and 30 K. Our results show that with decrease in temperature there is a decrement in the width of the core level peaks. This is very clearly observed in the case of Ba and O $1s$ core levels. The Bi and Pb $4f_{7/2}$ core levels exhibits two features labelled as A and A*. Such features have been observed in Bi core level spectra by Prachi et al.⁴² in the case of Bi based pyrochlore iridate where the sample is metallic and have attributed the features A and A* to be of poorly and well screened features. Such two features have also been observed in the case of Pb $4f_{7/2}$ by Payne et al.⁴³, in the case of PbO_2 sample that is metallic. It is interesting to note that in the case of BaBiO_3 , that is semi conducting, only poorly screened feature is observed^{44,45}. The well screened feature arises when the Bi/Pb $4f_{7/2}$ core hole is screened by the transfer of electrons from the ligand and the poorly screened feature arises when no such transfer occurs.

B. xps Valence Band and Band Structure Studies

The comparison of xps and HeII valence band spectra collected at 300 K is shown in figure 9. Finite DOS at E_F

is clearly visible in both xps and HeII spectra. We observe six features in the spectra labelled as A, B₁, B₂, B₃, C and D. The xps valence band represents the bulk features of the sample. To identify the features, band structure calculations were carried out on $\text{BaPb}_{0.75}\text{Bi}_{0.25}\text{O}_3$, in the tetragonal phase using DFT method, as shown in figure 10. Our results show that the total density of states (TDOS) of TB-mBJ is shifted towards lower energy as compared to the LDA calculations, as seen in panel (a) of figure 10. The partial density of states (PDOS) are plotted in panels (b)–(f) of figure 10. While LDA calculations generally sufficient in case of metallic compounds, it has been well documented that LDA underestimates the band gap at the fermi level^{46,47} of semiconducting or insulating compounds. This was the case of the parent compound, BaBiO_3 , where the gap obtained in the case of LDA calculations was underestimated as compared to the TB-mBJ calculations⁴⁴. However, the compound under study, $\text{BaPb}_{0.75}\text{Bi}_{0.25}\text{O}_3$, exhibits both metallic and semiconducting behaviours, as discussed previously. Further, we're also probing the effects of Pb doping in BaBiO_3 to understand how the band gap observed in BaBiO_3 closes upon Pb doing. Thus, TB-mBJ calculations have been employed to understand the electronic structure of $\text{BaPb}_{0.75}\text{Bi}_{0.25}\text{O}_3$. The experimental spectra were matched with the TB-mBJ calculations with a finite energy shift. Towards this, in the present work, a rigid shift of -0.8 eV was given to the DOS obtained from the TB-mBJ calculation to match with the experimental spectrum.

Our results show that there is finite DOS at the Fermi level that is in line with the experimental spectra. The calculated DOS can be divided into five regions. In region I (-14 to -12 eV), there is significant contribution from Ba $5p$ states and weak contributions from Bi/Pb $6s$ and Pb $6d$ states. Region II (-12 to -7 eV) covers dominant contributions from Bi/Pb $6s$ and weak contributions from rest of the DOS. Region III (-7eV to -1.5 eV) has contributions from Bi/Pb $6s$, $6p$, $6d$, $5f$ and O $2p$ states. In region IV (-1.5 to E_F) there is dominant contribution from Bi $6s$ and weak contributions from other states. The region V (above E_F to 2eV) has dominant contribution from Pb $6s$ and weak contributions from rest of the states. We now identify the different features based

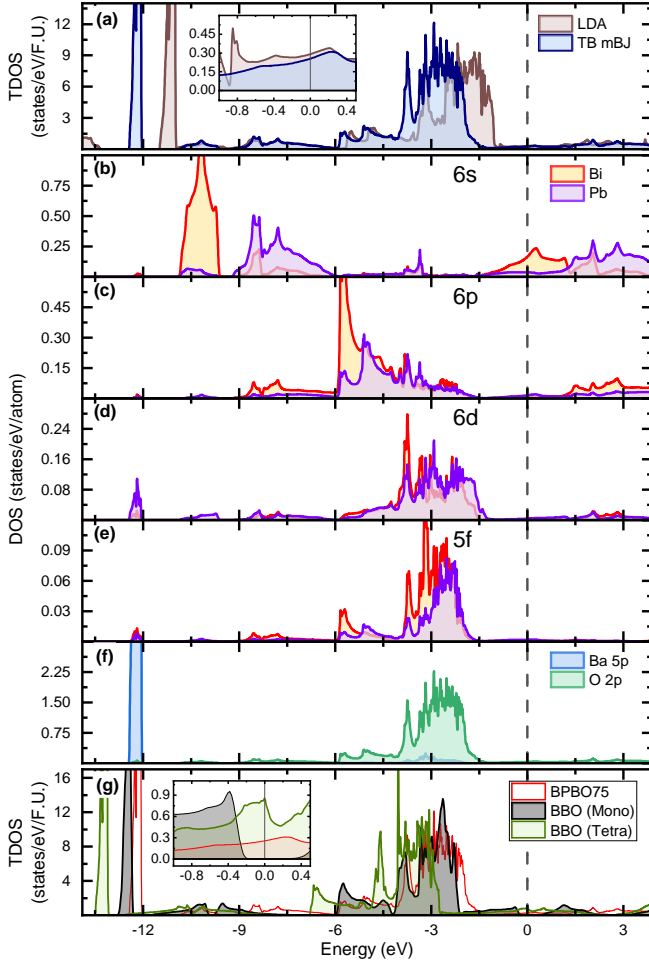


FIG. 10: (Color online) DFT calculations performed on tetragonal phase of $\text{BaPb}_{0.75}\text{Bi}_{0.25}\text{O}_3$. Panel (a) shows the comparison between LDA (brown) and TB-mBJ (blue) calculations; inset shows the region near E_F , where finite DOS is clearly visible; panels (b)–(e) show the partial DOS (PDOS) of Bi (red) and Pb (violet) 6s, 6p, 6d and 5f states, respectively obtained using TB-mBJ calculations; panel (f) shows the PDOS of Ba 5p (light blue) and O 2p (green) states obtained using TB-mBJ calculations. Panel (g) shows the TDOS obtained from the TB-mBJ calculations for BaBiO_3 in the monoclinic phase (black), $\text{BaPb}_{0.75}\text{Bi}_{0.25}\text{O}_3$ in the tetragonal phase (red), and BaBiO_3 using the structural parameters of $\text{BaPb}_{0.75}\text{Bi}_{0.25}\text{O}_3$ (green).

on the above results. The feature *D* represents surface cleanliness. In the case of xps, the intensity of this feature is low as compared to the HeII spectra due to higher sensitivity to surface oxygen. The features B_1 , B_2 and B_3 covers region III and the feature *A* encompasses region II. The photoionisation cross section for Al K_α source is more for Bi/Pb 6s as compared to the photoionisation cross section of O 2p, while in the case of HeII spectra, the reverse is true. Hence, the higher intensity of feature *A* observed in xps as compared to HeII spectra suggests the contributions from Bi/Pb 6s states.

Pb doping introduces a significant change in the elec-

tronic structure near E_F as compared to BaBiO_3 . An insulating gap at E_F observed in BaBiO_3 ⁴⁴ closes on 75% Pb doping. The region between -3 to -1.4 eV which was identified as feature *B* in BaBiO_3 ⁴⁴ splits into 3 features upon Pb doping, namely, B_1 , B_2 and B_3 . All the three features have dominant contributions from O 2p states. In figure 10 (g), we have presented the TB-mBJ calculations of monoclinic BaBiO_3 (labelled as BBO (Mono)), BaBiO_3 using the structural parameters of $\text{BaPb}_{0.75}\text{Bi}_{0.25}\text{O}_3$ (labelled BBO (Tetra)) and $\text{BaPb}_{0.75}\text{Bi}_{0.25}\text{O}_3$. By performing TB-mBJ calculations on BaBiO_3 using the structural parameters of $\text{BaPb}_{0.75}\text{Bi}_{0.25}\text{O}_3$, we intend to understand the origin of states at E_F . Our results show that there is finite DOS at E_F in this case. This suggests that the finite DOS appearing at E_F is mainly driven by the crystal structure. Further, the DOS at Fermi level was observed to decrease upon Pb doping, as seen clearly in the inset of figure 10 (g). To ascertain that the position of bismuth does not play an important role in the electronic structure of $\text{BaPb}_{0.75}\text{Bi}_{0.25}\text{O}_3$, we repeated the TB-mBJ calculations by substituting the bismuth atom in each of the different positions of lead. The total DOS was observed to be identical in all the cases.

C. UPS Valence Band Studies near E_F

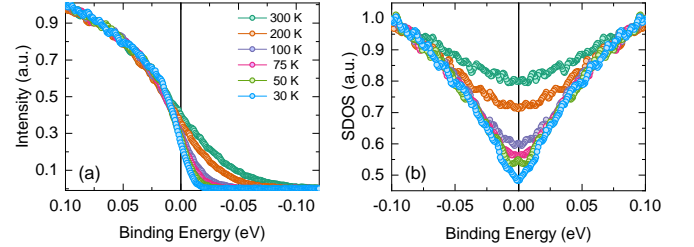


FIG. 11: (a) HeI Spectra of $\text{BaPb}_{0.75}\text{Bi}_{0.25}\text{O}_3$ collected at various temperatures in a narrow range; fermi level, E_F is at binding energy = 0 eV (b) Spectral DOS obtained from the symmetrization of the HeI spectra at different temperatures, shown in panel (a).

Having identified the states that contribute to the Fermi level (E_F), we now look into the evolution of the states close to E_F . In figure 11(a), we show the temperature dependent valence band collected using HeI spectra. All the spectra are normalised at 100 meV. Our results show that all the spectra show a finite intensity at E_F and this intensity is found to decrease on lowering the temperature. To observe more clearly the temperature behaviour of the states close to E_F , the spectral density of states was obtained by dividing the experimental spectra by the Fermi Dirac distribution and symmetrising it, figure 11(b). The figure shows significant reduction in the intensity as a dip in the vicinity of E_F with decrease in temperature. This dip increases as the tem-

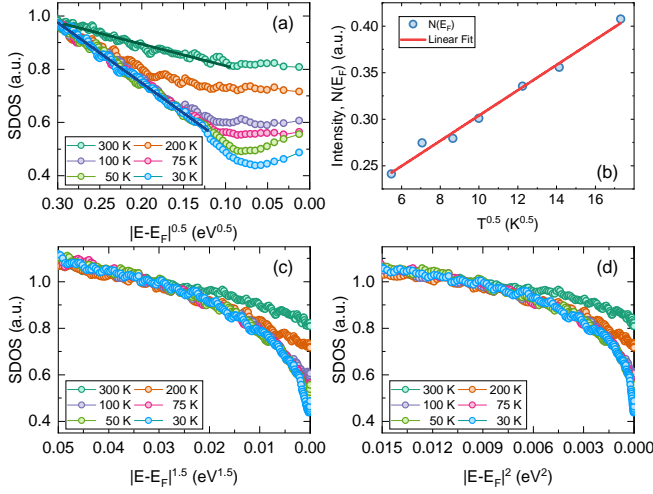


FIG. 12: (a) Spectral DOS (open circles) as a function of $|E - E_F|^{1/2}$, (b) Intensity at E_F , $N(E_F)$, as a function of $T^{1/2}$ (open circles). The linear fit (solid lines) to SDOS in panel (a) and $N(E_F)$ in panel (b) indicate that the sample is a disordered metal. (c) SDOS (open circles) as a function of $|E - E_F|^{3/2}$, and (d) SDOS (open circles) as a function of $|E - E_F|^2$.

perature drops and a systematic increase in the spectral DOS above 100 meV is observed with decrease in temperature suggesting the stabilization of pseudogap.

It is important to note that Matsuyama et al.¹⁷ have collected He I and II spectra on $\text{BaPb}_{0.85}\text{Bi}_{0.15}\text{O}_3$ at around 300 K and 180 K. Based on the Fermi edge observed in this compound, they proposed that the superconductivity would be driven by cooper pairing of electrons in Fermi liquid states. To check for this possibility, the SDOS was plotted as a function of $(E - E_F)^n$. Our results show that the value of n thus obtained was 0.5 suggesting the role of disorder existing in the compound, as seen in figure 12(a). Earlier studies^{48,49} have shown that such decrement in the intensity could arise due to the localization of the states at E_F induced by disorder. Under this situation, it is expected that the DOS at E_F follows $N(E_F) = a + b\sqrt{T}$, where T is the temperature; such a behaviour can be clearly observed in panel (b) of figure 12, thus suggesting that the compound is a disordered metal for $T > T_C$. However, to observe whether there is any characteristic peak observed close to E_F representing the superconducting state, experiments below T_C are required.

VI. SUMMARY

In conclusion, we have studied the structural, transport and electronic properties of the polycrystalline superconducting $\text{BaPb}_{0.75}\text{Bi}_{0.25}\text{O}_3$ sample. The analysis of the temperature dependent resistivity data reveals the compound undergoes a superconducting transition around 11 K. The VRH behaviour of the resistivity at low temperatures in an indication that disorder plays a very important role in the electronic properties of the compound. We believe that the structural dimorphism present in the sample at all temperatures, along with the coexistence of metallic and semiconducting regions in the sample are the likely causes for disorder in the compound under study. To explore the effect of phase separation, structural studies were conducted using *xrd* which reveal that the compound is dimorphic at all temperatures ranging from 300 K down to 10 K. Further, the evolution of the tetragonal and orthorhombic strain with temperature indicate that the strain is maximum as we approach the T_C . The observation of well screened features in the Bi and Pb spin orbit split 4f core level suggests the metallic nature of the sample. Additionally, we observed a finite density of states at Fermi level. Our band structure studies suggest that the closing of the gap upon Pb doping is due to structural transition from the monoclinic I2/m phase to the tetragonal I4/mcm phase. The temperature-dependent behaviour of the electronic states close to the fermi level was studied using UPS measurements. The signature of disorder was observed in the form of $|E - E_F|^{1/2}$ dependence of SDOS near the Fermi level suggests the compound under study for $T > T_C$ is a disordered metal. Furthermore, the DOS at Fermi level decreased progressively with temperature – an evidence of opening of disorder-induced pseudogap. Our combined crystal structure, transport and electronic structure studies suggest that lattice strain and disorder act as precursor to superconductivity in $\text{BaPb}_{0.75}\text{Bi}_{0.25}\text{O}_3$ compound.

VII. ACKNOWLEDGEMENTS

The authors, Bharath M and R Bindu thank Science and Engineering Research Board (SERB), Department of Science and Technology, Government of India for funding this work. This work is funded under the SERB project sanction order No. EMR-2016-001144.

¹ E. Climent-Pascual, N. Ni, S. Jia, Q. Huang, and R. Cava, Physical Review B **83**, 174512 (2011).

² A. W. Sleight, J. Gillson, and P. Bierstedt, Solid State Communications **88**, 841 (1993).

³ T. D. Thanh, A. Koma, and S. Tanaka, Applied Physics **22**, 205 (1980).

⁴ D. Marx, P. Radaelli, J. Jorgensen, R. Hitterman, D. Hinks, S. Pei, and B. Dabrowski, Physical Review B **46**, 1144 (1992).

⁵ D. Nicoletti, E. Casandruc, D. Fu, P. Giraldo-Gallo, I. Fisher, and A. Cavalleri, Proceedings of the National Academy of Sciences **114**, 9020 (2017).

- ⁶ C. Parra, F. C. Niestemski, A. W. Contryman, P. Giraldo-Gallo, T. H. Geballe, I. R. Fisher, and H. C. Manoharan, *Proceedings of the National Academy of Sciences* **118**, e2017810118 (2021).
- ⁷ J. Kim, J. Mun, B. Kim, H. G. Lee, D. Lee, T. H. Kim, S. Lee, M. Kim, S. H. Chang, and T. W. Noh, *Physical Review Materials* **3** (2019), URL <https://doi.org/10.1103/2Fphysrevmaterials.3.113606>.
- ⁸ D. Cox and A. Sleight, *Solid State Communications* **19**, 969 (1976).
- ⁹ Y. d. Khan, K. Nahm, M. Rosenberg, and H. Willner, *physica status solidi (a)* **39**, 79 (1977).
- ¹⁰ M. Oda, Y. Hidaka, A. Katsui, and T. Murakami, *Solid state communications* **55**, 423 (1985).
- ¹¹ H. Asano, M. Oda, Y. Endoh, Y. Hidaka, F. Izumi, T. Ishigaki, K. Karahashi, T. Murakami, and N. Watanabe, *Japanese journal of applied physics* **27**, 1638 (1988).
- ¹² M. Oda, Y. Hidaka, A. Katsui, and T. Murakami, *Solid State Communications* **60**, 897 (1986), ISSN 0038-1098, URL <https://www.sciencedirect.com/science/article/pii/0038109886903819>.
- ¹³ P. Giraldo-Gallo, Y. Zhang, C. Parra, H. Manoharan, M. Beasley, T. Geballe, M. Kramer, and I. Fisher, *Nature communications* **6**, 1 (2015).
- ¹⁴ K. Luna, P. Giraldo-Gallo, T. Geballe, I. Fisher, and M. Beasley, *Physical Review Letters* **113**, 177004 (2014).
- ¹⁵ D. T. Harris, N. Campbell, R. Uecker, M. Brützm, D. G. Schlom, A. Levchenko, M. S. Rzchowski, and C.-B. Eom, *Physical Review Materials* **2**, 041801 (2018).
- ¹⁶ G. Wertheim, J. Remeika, and D. Buchanan, *Physical Review B* **26**, 2120 (1982).
- ¹⁷ H. Matsuyama, T. Takahashi, H. Katayama-Yoshida, Y. Okabe, H. Takagi, and S. Uchida, *Physical Review B* **40**, 2658 (1989).
- ¹⁸ A. Winiarski, G. Wübbeler, C. Scharfschwerdt, E. Clausen, and M. Neumann, *Fresenius' journal of analytical chemistry* **341**, 296 (1991).
- ¹⁹ H. Namatame, A. Fujimori, H. Takagi, S. Uchida, F. De Groot, and J. Fuggle, *Physical Review B* **48**, 16917 (1993).
- ²⁰ H. Sakamoto, H. Namatame, T. Mori, K. Kitazawa, S. Tanaka, and S. Suga, *Journal of the Physical Society of Japan* **56**, 365 (1987).
- ²¹ G. Kostikova, D. Korol'Kov, and Y. P. Kostikov, *Russian journal of general chemistry* **71**, 1010 (2001).
- ²² D. V. Korolkov, G. P. Kostikova, and Y. P. Kostikov, *Physica C: Superconductivity* **383**, 117 (2002).
- ²³ T. Hashimoto and H. Kawazoe, *Solid state communications* **87**, 251 (1993).
- ²⁴ *Elk software*, URL <https://elk.sourceforge.net/>.
- ²⁵ J. P. Perdew and Y. Wang, *Physical Review B* **45**, 13244 (1992).
- ²⁶ F. Tran and P. Blaha, *Physical Review Letters* **102**, 226401 (2009).
- ²⁷ S. Uchida, H. Hasegawa, K. Kitazawa, and S. Tanaka, *Physica C: Superconductivity* **156**, 157 (1988).
- ²⁸ T. Hashimoto, H. Kawazoe, and H. Shimamura, *Physica C: Superconductivity* **223**, 131 (1994).
- ²⁹ J. Schnakenberg, *Physica Status Solidi (b)* **28**, 623 (1968), URL <https://doi.org/10.1002/2Fpssb.19680280220>.
- ³⁰ G. Greaves, *Journal of Non-Crystalline Solids* **11**, 427 (1973).
- ³¹ R. Kumar, R. Choudhary, M. Ikram, D. Shukla, S. Mollah, P. Thakur, K. Chae, B. Angadi, and W. Choi, *JOURNAL OF APPLIED PHYSICS* **102**, 073707 (2007).
- ³² S. Uchida, K. Kitazawa, and S. Tanaka, *Phase transitions* **8**, 95 (1987).
- ³³ N. Mott, *Philosophical Magazine* **26**, 1015 (1972).
- ³⁴ N. F. Mott and E. A. Davis, *Electronic processes in non-crystalline materials* (Oxford university press, 2012).
- ³⁵ R. Rosenbaum, *Physical Review B* **44**, 3599 (1991).
- ³⁶ H. Sakata, K. Seg, and B. K. Chaudhuri, *Physical Review B* **60**, 3230 (1999), URL <https://doi.org/10.1103/2Fphysrevb.60.3230>.
- ³⁷ K. Kitazawa, S. Uchida, and S. Tanaka, *Physica B+ C* **135**, 505 (1985).
- ³⁸ O. Chmaissem, B. Dabrowski, S. Kolesnik, J. Mais, J. Jorgensen, and S. Short, *Physical Review B* **67**, 094431 (2003).
- ³⁹ P. Sharma, S. Pathak, H. Pant, and R. Bindu, *Applied Physics A* **128**, 271 (2022).
- ⁴⁰ A. Patterson, *Physical review* **56**, 978 (1939).
- ⁴¹ P. Horn, D. Keane, G. Held, J. Jordan-Sweet, D. Kaiser, F. Holtzberg, and T. Rice, *Physical review letters* **59**, 2772 (1987).
- ⁴² P. Telang, A. Bandyopadhyay, K. Mishra, D. Rout, R. Bag, A. Gloskovskii, Y. Matveyev, and S. Singh, *Journal of Physics: Condensed Matter* **34**, 395601 (2022).
- ⁴³ D. J. Payne, R. G. Egdell, D. S. Law, P.-A. Glans, T. Learmonth, K. E. Smith, J. Guo, A. Walsh, and G. W. Watson, *Journal of Materials Chemistry* **17**, 267 (2007).
- ⁴⁴ M. Bharath, P. Sharma, J. Brar, R. Maurya, and R. Bindu, *Journal of Physics: Condensed Matter* **32**, 055504 (2019).
- ⁴⁵ N. Plumb, D. Gawryluk, Y. Wang, Z. Ristić, J. Park, B. Lv, Z. Wang, C. Matt, N. Xu, T. Shang, et al., *Physical Review Letters* **117**, 037002 (2016).
- ⁴⁶ J. P. Perdew and M. Levy, *Physical Review Letters* **51**, 1884 (1983).
- ⁴⁷ L. J. Sham and M. Schlüter, *Physical review letters* **51**, 1888 (1983).
- ⁴⁸ D. Sarma, A. Chainani, S. Krishnakumar, E. Vescovo, C. Carbone, W. Eberhardt, O. Rader, C. Jung, C. Hellwig, W. Gudat, et al., *Physical review letters* **80**, 4004 (1998).
- ⁴⁹ M. Kobayashi, K. Tanaka, A. Fujimori, S. Ray, and D. Sarma, *Physical review letters* **98**, 246401 (2007).